Modeling coupled erosion and filtration of fine particles in granular media

Jie YANG[1,2], Zhen-Yu YIN[2,3], Farid LAOUAFA[1,*], Pierre-Yves HICHER[2]

Affiliations:

[1]INERIS, Verneuil en Halatte, France

[2]Research Institute of Civil Engineering and Mechanics (GeM), UMR CNRS 6183, Ecole Centrale de Nantes, France

[3]Key Laboratory of Geotechnical and Underground Engineering of Ministry of Education; Department of Geotechnical Engineering, College of Civil Engineering, Tongji University, Shanghai, China

*Corresponding authors: Dr. Farid LAOUAFA, Tel.: +33 344556182, Email: farid.laouafa@ineris.fr

Abstract: One of the major causes of instability in geotechnical structures such as dikes or earth dams is the phenomenon of suffusion including detachment, transport and filtration of fine particles by water flow. Current methods fail to capture all these aspects. This paper suggests a new modeling approach under the framework of the porous continuous medium theory. The detachment and transport of the fine particles are described by a mass exchange model between the solid and the fluid phases. The filtration is incorporated to simulate the filling of the inter-grain voids created by the migration of the fluidized fine particles with the seepage flow and, thus, the self-filtration is coupled with the erosion process. The model is solved numerically using a finite difference method restricted to one-dimensional (1-D) flows normal to the free surface. The applicability of the model to capture the main features of both erosion and filtration during the suffusion process has been validated by simulating 1-D internal erosion tests and by comparing the numerical with the experimental results. Furthermore, the influence of the coupling between erosion and filtration has been highlighted, including the development of material heterogeneity induced by the combination of erosion and filtration.

Keywords: granular media, internal erosion, suffusion, filtration, permeability, seepage

1. Introduction

Internal erosion is a significant issue in civil and environmental engineering impacting the safety of dams and dikes. Statistical analyses of accidents in embankment dams indicate that the two main causes [1-3] of failure are internal erosion and overtopping. Meanwhile, recent studies indicate that internal erosion is also an important issue in underground structures, such as land subsidence due to water piping induced erosion [4], lateral displacement induced by erosion during jet grouting [5], surface settlement induced by erosion because of tunnel leakage [6], and landslides or slope instability induced by fines migration under rainfull condition [7,8]. Four forms of internal erosion have been distinguished [2,9-11]: concentrated leak erosion, backward erosion, contact erosion and suffusion. Among them, suffusion is a complex phenomenon appearing as a combination of detachment and transport of the finer particles driven by water flow, with possible filtration within the voids between coarser particles. As a result, the particle size distribution, the porosity, and the hydraulic conductivity of the soil are changed. The mechanical properties of the soil are, therefore, progressively degraded with time, which causes the hydraulic earth structures to face a considerable risk of failure [12-14]. Thus, to ensure the safety assessment of earth structures, suffusion has been widely studied by laboratory testing over the last few decades, focusing on the effect of soil grading, critical hydraulic gradient, critical pore water velocity, with the purpose of characterizing the susceptibility of soils to suffusion [15-26]. Several criterions have been proposed to evaluate the internal stability of gap-graded or broadly graded granular materials [27-30]. Extensive theoretical works have also been performed to study the fines migration in the applications of petroleum engineering [31-33].

Based on these experimental findings, many constitutive models have been proposed under the framework of the porous continuous medium theory to enhance the design of hydraulic earth structures [32,34-39]. Most of these models can describe the detachment and transport of finer soil particles within the solid matrix induced by erosion [15-22]. However, recent studies revealed that erosion is usually accompanied by self-filtration and clogging [35,40,41]. Self-filtration and clogging represent a similar phenomenon, which is the filling of the initial voids due to the migration of the fluidized fine particles with the seepage flow. It is induced within the specimen or near the outlet, and results in a decrease in hydraulic conductivity. Therefore, both erosion and filtration should be considered in the modeling of suffusion.

More recently, the discrete approach has been applied in the studies of fines migration [42-47]. For instance, Zou et al. [48] applied the coupled discrete element method and computational fluid dynamics technique to simulate the transient transport of eroded base-soil particles into a filter. Wang et al. [49] applied the coupled bonded particle and lattice Boltzmann method to investigate the erosion process of soil particles in granular filters. The microscopic migration of soil particles can be clearly visualized. The discrete methods can represent fairly well the microstructure and describe better and better the physical mechanisms within granular materials. However, they are still restricted to problems with a limited number of particles which is far from real engineering structures. The continuous approach is thus strongly recommended for solving boundary value problems.

Therefore, this paper attempts to formulate a new numerical approach considering both erosion and filtration in suffusion under the framework of the porous continuous medium theory. First, four-constituent based mass exchange formulations are proposed to describe the detachment of finer particles and the clogging of initial voids. The coupling formulations are solved numerically by a finite difference method. Then, the model is validated by simulating 1-D internal erosion tests by demonstrating that it can reproduce the main features of both erosion and filtration during the suffusion process. The influence of the coupling between erosion and filtration is further studied.

2. Model formulations

2.1. Mass exchange and mass balance equations

According to [39], it is possible to consider the saturated porous medium as a material system composed of 4 constituents: the stable fabric of the solid skeleton (*ss*), the erodible fines (*se*), the fluidized particles (*fp*) and the pure fluid phase (*ff*), as shown in Fig. 1. The fines can behave either as a fluid-like (described as fluidized particles) or as a solid-like (described as erodible fines) material. Thus, a liquid-solid phase transition process has been accounted for in the present model by the introduction of a mass and volume production term into the corresponding mass and volume balances for erodible fines (*se*) and fluidized particles (*fp*).

(a) Micro-scale (b) 4 constituents

Fig. 1 REV of a fully-saturated soil mixture and the four-constituent continuum model

In a given Representative Elementary Volume (REV), dV, constituted by the four constituents, the volume fraction of a single constituent i is expressed as follows:

$$n^i\left(x,t\right)=\frac{\mathrm{d}V^i\left(x,t\right)}{\mathrm{d}V} \tag{1}$$

with $i=\left\{ss, se, ff, fp\right\}$ denoting the 4 constituents, V^i denoting the volume of the corresponding constituent.

At a material point level, the mass balance for the i phase is given, neglecting the hydro-mechanical dispersion tensor, by Schaufler et al. [39]:

$$\frac{\partial\left(\rho^i\right)}{\partial t}+\mathrm{div}\left(\rho^i\mathbf{v}^i\right)=\rho^{ex,i} \tag{2}$$

where $\rho^{ex,i}$ and $\mathbf{v}^i$ denote, respectively, the mass exchange term and the velocity of the corresponding constituent. The partial density ρ^i is defined as the ratio between the mass $\mathrm{d}m^i$ of the constituent i with respect to the total volume dV of the REV, leading to a relation between partial densities ρ^i and effective densities ρ^{iR}, which corresponds to the bulk density of the corresponding constituents:

$$\rho^i=\frac{\mathrm{d}m^i}{\mathrm{d}V}=\frac{\mathrm{d}m^i}{\mathrm{d}V^i}\frac{\mathrm{d}V^i}{\mathrm{d}V}=\rho^{iR}n^i \tag{3}$$

The mass balances for the four constituents are then reduced to the corresponding volume fraction balance:

$$\frac{\partial\left(n^i\right)}{\partial t}+\mathrm{div}\left(n^i\mathbf{v}^i\right)=n^{ex,i} \tag{4}$$

$n^{ex,i}$ is the term of the volume of mass exchange to be discussed in the following section.

Moreover, it is assumed that fluid and fluidized particles have at any time and at a given point the same velocity. The solid skeleton is assumed to be deformable but non-erodible. The porosity field $\phi(x,t)$, the amount of erodible fines $f_c(x,t)$ and the concentration of the fluidized particles $c(x,t)$ are defined as follows:

$$\phi = \frac{\mathrm{d}V_v}{\mathrm{d}V} = \frac{\mathrm{d}V^{ff} + \mathrm{d}V^{fp}}{\mathrm{d}V} = n^{ff} + n^{fp} \tag{5}$$

$$f_c = \frac{n^{se}}{n^{ss} + n^{se}} = \frac{n^{se}}{1-\phi} \tag{6}$$

$$c = \frac{n^{fp}}{n^{ff} + n^{fp}} = \frac{n^{fp}}{\phi} \tag{7}$$

The phase transition of the fine particles from solid to fluidized particles leads to:

$$-n^{ex,fp} = n^{ex,se} = n,\ n^{ex,ss} = 0,\ n^{ex,ff} = 0 \tag{8}$$

The mass balance equations are then given by the following expressions:

$$-\frac{\partial \phi}{\partial t} + \mathrm{div}(\mathbf{v}_s) - \mathrm{div}(\phi \mathbf{v}_s) = n \tag{9}$$

$$\frac{\partial(f_c)}{\partial t} - \frac{\partial(f_c\phi)}{\partial t} + \mathrm{div}(f_c\mathbf{v}_s) - \mathrm{div}(f_c\phi\mathbf{v}_s) = n \tag{10}$$

$$\frac{\partial(c\phi)}{\partial t} + \mathrm{div}(c\mathbf{q}_\mathbf{w}) + \frac{\partial(c\phi\mathbf{v}_s)}{\partial t} = -n \tag{11}$$

$$\mathrm{div}(\mathbf{q}_w) + \mathrm{div}(\mathbf{v}_s) = 0 \tag{12}$$

where $\mathbf{q}_\mathbf{w}$ denotes the volume discharge rate (the volume of flow through the unit cross-sectional area in unit time):

$$\mathbf{q}_\mathbf{w} = \phi(\mathbf{v}_f - \mathbf{v}_s) \tag{13}$$

$$\mathbf{v}_s = \frac{\partial \mathbf{u}(x,t)}{\partial t} \tag{14}$$

with $\mathbf{u}(x.t)$ indicating the displacement field of the soil skeleton. The strain ε_{ij} and volumetric strain ε_v are then given by the following expressions under small strain assumption:

$$\varepsilon_{ij} = -\frac{1}{2}\left(u_{i,j} + u_{j,i}\right) \tag{15}$$

$$\frac{\partial(\varepsilon_v)}{\partial t} = -\mathrm{div}(\mathbf{v}_s) \tag{16}$$

This study focuses on the erosion-clogging process, in which only elastic model is used to calculate the displacement field according to the change of effective stress due to the pore pressure evolution. The selected experimental tests presented later on are also only under hydraulic loadings for this purpose. Note that the irreversible coupling from mechanics to hydraulics has already been considered implicitly by introducing the volume deformation in the mass balance equations Eq. (9)-(12), the mechanical coupling can be easily implemented if the elastic model is replaced by elastoplastic models. For the cases with external mechanical loadings, the strength degradation induced by the evolution of the porosity and the fines may then be captured which will be discussed in future studies.

Eq.(9) describes the behavior of the solid phase (solid skeleton and erodible fines). Eq.(10) represents the balance of volume of the erodible fines, whereas Eq.(11) is the balance of volume of the fluidized particles. The balance of the mass of the mixture, *i.e.*, the continuity equation, is given by Eq.(12).

Note that the amount of erodible fines f_c can be obtained explicitly from the current porosity ϕ and the volumetric strain ε_v, which indicates that Eq.(10) can be replaced by :

$$f_c = 1 - \frac{(1+\varepsilon_v)(1-\phi_0)(1-f_{c0})}{1-\phi} \tag{17}$$

where $\phi_0(x)$ and $f_{c0}(x)$ denote the initial value of $\phi(x,t)$ and $f_c(x,t)$, respectively.

2.2. Coupling of erosion and filtration

The variable n in Eqs.(9)-(12) is the volume of mass exchange, which corresponds to the rate of eroded mass volume (n_e) and filtrated mass volume (n_f) at any time and any point.

$$n = n_e + n_f \tag{18}$$

A model for the rate of the eroded mass is given by the relation [50]:

$$n_e = -\lambda_e (1-\phi)(f_c - f_{c\infty})|\mathbf{q_w}| \tag{19}$$

where $f_{c\infty}$ is the ultimate fine content fraction after a long seepage period, λ_e is a material parameter. The ultimate fine content fraction $f_{c\infty}$ is assumed to be decreasing with the increase of the hydraulic gradient [51] as

$$f_{c\infty} = f_{c0}\left[(1-\alpha_1)\exp\left(-|\mathbf{q_w}|\times 10^{\alpha_2}\right)+\alpha_1\right] \tag{20}$$

where f_{c0} is the initial fine content fraction, α_1 and α_2 are material parameters. The term $(f_c - f_{c\infty})$ in Eq.(19) corresponds to the residual fine content fraction. The erosion rate depends not only on the total discharge of liquid $\mathbf{q_w}$ but also on the residual fine content fraction as shown by Eq.(19).

It is assumed that, with an increasing concentration of transported fine particles, the probability of the existence of the filtration phenomenon in the system of pore canals will also increase. The following model for the rate of the filtrated mass is suggested:

$$n_f = \lambda_f \frac{\phi - \phi_{\min}}{\phi^{\beta}} c|\mathbf{q_w}| \tag{21}$$

where λ_f and β are material parameters, $\phi_{\min}$ is the minimum porosity of the soil mixture. The probability of filtration increases with an increasing discharge of the fluidized particles ($c|\mathbf{q_w}|$). Moreover, the filtration process is expected to be more intense in intact regions, which are characterized by smaller pore canals, i.e. smaller porosity. β is related to the heterogeneity of the soil mixture, which is discussed in the following section.

2.3. One-dimensional suffusion process

This paper focuses on one-dimensional suffusion problems along the x axis, chosen normal to the free surface and pointing downward into the interior of the specific finite domain (see Fig. 2).

The flow in the porous medium is governed by Darcy's law which states that the flow rate is driven by the gradient of the pore fluid pressure:

$$q_w = -\frac{k\left(f_c,\phi\right)}{\eta_k \bar{\rho}\left(c\right)} \frac{\partial\left(p_w\right)}{\partial x} \tag{22}$$

where $k\left(f_c,\phi\right)$ denotes the intrinsic permeability of the medium, η_k is the kinematic viscosity of the fluid, p_w is the pore fluid pressure, and $\bar{\rho}\left(c\right)$ is the density of the mixture defined as:

$$\bar{\rho} = c\rho_s + \left(1-c\right)\rho_f \tag{23}$$

with ρ_s the density of the solid and ρ_f the density of the fluid. For a mixture, the intrinsic permeability $k\left(x,t\right)$ of the porous medium depends on the current porosity $\phi\left(x,t\right)$ and on the fine content fraction as [52]:

$$k = k_0\left(1-\varphi_v\right)^{3m} \tag{24}$$

where m is the so-called "cementation exponent" and varies with the pore geometry. A high value of the cementation exponent indicates a strong decoupling between the total interconnected porosity and the effective porosity that controls the flow. $\varphi_v\left(x,t\right)$ is the volume fraction of the fine content:

$$\varphi_v = f_c\left(1-\phi\right) \tag{25}$$

Therefore, by combining Eqs. (9)-(25), the governing equations for the pore pressure $p_w\left(x,t\right)$, the porosity $\phi\left(x,t\right)$ and the concentration of fluidized particles $c\left(x,t\right)$ can be expressed as follows under one-dimensional condition:

$$\frac{\partial\left(p_w\right)}{\partial t} - \frac{Ek\left(f_c,\phi\right)}{\eta\bar{\rho}\left(c\right)} \frac{\partial^2\left(p_w\right)}{\partial x^2} = 0 \tag{26}$$

$$\frac{\partial\phi}{\partial t} + \frac{\partial u}{\partial t}\frac{\partial\phi}{\partial x} - \frac{\partial\varepsilon_v}{\partial t}\phi + \frac{\partial\varepsilon_v}{\partial t} + \left(-\lambda_e\left(1-\phi\right)\left(f_c - f_{c\infty}\right) + \lambda_f \frac{\phi-\phi_{\min}}{\phi^{\beta}}c\right)\left|q_w\right| = 0 \tag{27}$$

$$\frac{\partial c}{\partial t}+\left(\frac{q_w}{\phi}+\frac{\partial u}{\partial t}\right)\frac{\partial c}{\partial x}+\frac{1}{\phi}\left[\frac{\partial \phi}{\partial t}+\operatorname{div}\left(q_w\right)+\frac{\partial \phi}{\partial x}\frac{\partial u}{\partial t}-\phi\frac{\partial \varepsilon_v}{\partial t}\right]c$$
$$+\frac{1}{\phi}\left(-\lambda_e\left(1-\phi\right)\left(f_c-f_{c\infty}\right)+\lambda_f\frac{\phi-\phi_{\min}}{\phi^{\beta}}c\right)\left|q_w\right|=0 \quad (28)$$

The coupled non-linear problem is supplemented by the following boundary and initial conditions:

$$p_w\left(x_0,t\right)=p_0,\ \ p_w\left(x_L,t\right)=p_L,\ c\left(x_0,t\right)=c_0,\ \frac{\partial c\left(x_L,t\right)}{\partial t}=0 \quad (29)$$

$$p_w\left(x,0\right)=0,\ c\left(x,0\right)=0,\ \phi\left(x,0\right)=\phi_0\left(x\right),\ f_c\left(x,0\right)=f_{c0}\left(x\right) \quad (30)$$

The initial porosity and the initial fine content depend on the homogeneity of the soil, which can vary along the space.

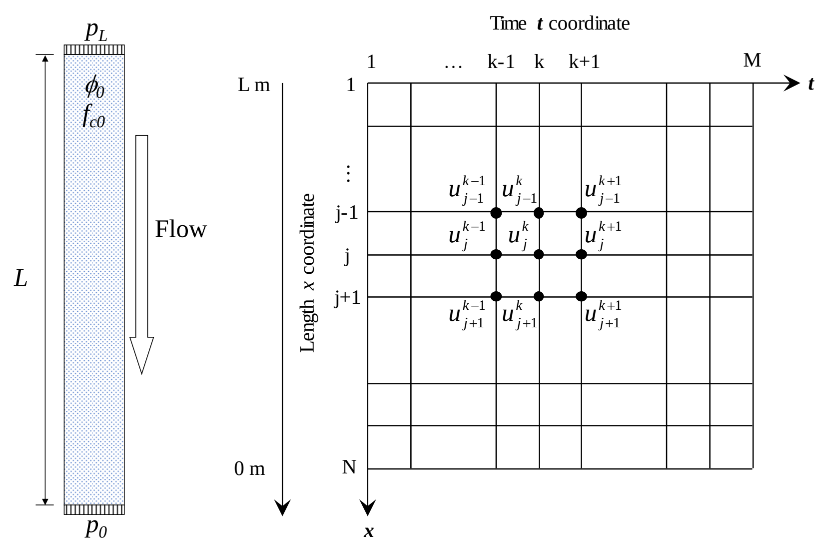

Fig. 2 Geometry and finite difference grid in space-time of analyzed 1-D internal erosion

3. Finite difference based numerical solution

Eqs. (26)-(28) make up an unsteady, coupled non-linear system of partial differential equations. The current state of the system depends on its previous state. The primary unknowns are the pore pressure $p_w\left(x,t\right)$, the porosity $\phi\left(x,t\right)$, and the transport concentration $c\left(x,t\right)$. Other unknowns such as displacement $u\left(x,t\right)$, attached fine content $f_c\left(x,t\right)$ and flow rate $q_w\left(x,t\right)$ can be determined explicitly by Eqs. (15), (17) and (22).

This system of partially differential equations has been solved through an explicit finite difference procedure. With the terminology shown in Fig. 2, Eqs. (26)-(28) become

$$\frac{p_{w\,j}^{\;k+1}-p_{w\,j}^{\;k}}{\Delta t}-\frac{\left[A_{p_w}\right]_{j+1/2}^{k}\left(p_{w\,j+1}^{\;k+1}-p_{w\,j}^{\;k+1}\right)+\left[A_{p_w}\right]_{j-1/2}^{k}\left(p_{w\,j}^{\;k+1}-p_{w\,j-1}^{\;k+1}\right)}{\left(\Delta x\right)^{2}}=0 \qquad (31)$$

$$\frac{\phi_j^{k+1}-\phi_j^{k}}{\Delta t}+\left[A_\phi\right]_j^k\frac{\phi_j^{k+1}-\phi_{j-1}^{k+1}}{\Delta x}+\left[B_\phi\right]_j^k\phi_j^k+\left[C_\phi\right]_j^k=0 \qquad (32)$$

$$\frac{c_j^{k+1}-c_j^{k}}{\Delta t}+\left[A_c\right]_j^k\frac{c_j^{k+1}-c_{j-1}^{k+1}}{\Delta x}+\left[B_c\right]_j^k c_j^k+\left[C_c\right]_j^k=0 \qquad (33)$$

where the subscripts $j\left(0,1...,N\right)$ represent the variation in length, described by the x co-ordinate, and the subscripts $k\left(0,1...,M\right)$ represent the variation in the time t co-ordinate. $k\left(f_c,\phi\right)$, $\bar{\rho}\left(c\right)$ and $q_w\left(x,t\right)$ vary with depth and time. As a simple approximation, their values at $\left(j,k\right)$ are used. A, B and C are equation coefficients given in Appendix A.

Eqs. (31)-(33) can then be solved with initial and boundary conditions for $p_w\left(x,t\right)$, $\phi\left(x,t\right)$, $c\left(x,t\right)$ given in Eqs. (29)-(30). The model has been coded with MATLAB software [53]. To obtain accuracy and run-time efficiency, the sensitivity of the results to space and time increments was examined. The computations of the following sections were carried out with $\Delta x=5\times10^{-4}\mathrm{m}$ (100 nodes) and 2000 increments in time.

4. Numerical simulations of laboratory tests

Two series of erosion tests on cohesionless soils were selected to examine the model performances: (1) Series A: Rochim et al. [23] performed hydraulic-gradient controlled downward erosion tests on gap-graded sand and gravel mixtures to evaluate the effects of the hydraulic loading history on the suffusion susceptibility of cohesionless soils, and (2) Series B: Aboul Hosn [54] performed flow-rate controlled downward erosion tests on gap-graded mixtures of coarse and fine silica Hostun sand in order to investigate the effects of the soil density on suffusion.

4.1. Series A

4.1.1. Review of experiments

The experimental set-up consisted of a modified triaxial cell surrounded by a steel mold to ensure the oedometric condition, a pressurized water supply system, and a water/soil collecting system. The specimens of 50 mm in diameter and 50 mm in height were prepared by using a single layer semi-static compaction technique, and then placed on a 4 mm pore opening grid to allow the migration of all sand particles. Two values of the initial dry density were targeted: 90% and 97% of the optimum Proctor density. After saturating the sample with an upward interstitial flow, the fluid was forced through the sample in the downward direction during the erosion test. Three gap-graded sand-gravel mixtures with different initial fine contents (20% for soil A, 25% for soil B and 29% for soil C) under two different hydraulic loadings were simulated. Fig. 3 shows the time evolution of the applied hydraulic gradients. The first multi-stage hydraulic gradient condition (named a) consisted of increasing the hydraulic gradient by steps of 0.1, 0.15, 0.2 and 0.25 up to 0.5, 0.8, 1 and 2, respectively, then by steps of 0.5 between 2 and 4 and by steps of 1 beyond 4. For the second kind of hydraulic loading named (b), the hydraulic gradient increment was directly imposed equal to 1. For both hydraulic loadings, each stage of the hydraulic gradient was kept constant for 10 min. Table 2 summarizes the initial dry density and initial permeability of the tested specimens, the values of the applied hydraulic gradient, and the duration of each test.

Table 1 properties of simulated test specimens

Soil reference	Specimen reference	Initial dry density γ_d (kN/m^3)	Initial permeability k (m/s)	Applied hydraulic gradient, *i*	Test duration (min)
A	A90-a	17.39	1.2×10^{-5}	Type a, from 0.1 to 15	270
	A90-b	17.39	2.0×10^{-5}	Type b, from 1 to 13	130
B	B97-a	18.74	1.3×10^{-5}	Type a, from 0.1 to 12	240
	B97-b	18.74	2.0×10^{-5}	Type b, from 1 to 9	90
C	C97-a	18.74	1.2×10^{-5}	Type a, from 0.1 to 9	210
	C97-b	18.74	2.0×10^{-5}	Type b, from 1 to 7	70

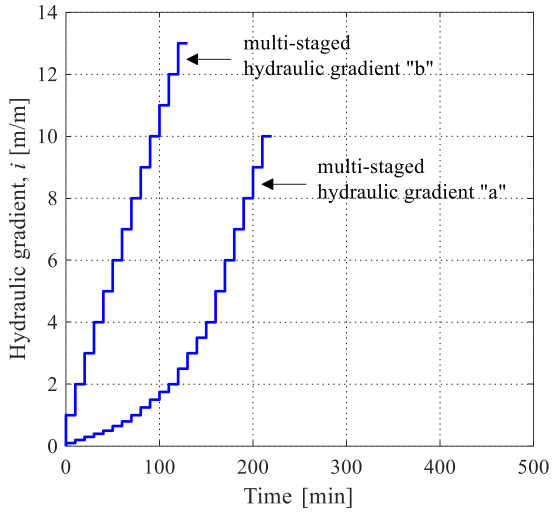

Fig. 3 Time evolution of multi-staged hydraulic gradients

The physical properties of the soil mixtures are summarized in Table 2, taken directly from the referred laboratory test [23]. The erosion parameters (λ_e, α_1 and α_2), filtration parameters (λ_f and β) and permeability parameter (m) were calibrated by fitting the evolution of the hydraulic conductivity and the cumulative loss of dry mass of soil mixture C (shown by the blue lines in Fig. 4) simultaneously in the case of hydraulic loadings (a) and (b), by trial-error which can also be identified using optimization technique [55,56]. All the values determined for the model parameters, summarized in Table 3, were used to predict the other tests.

Table 2 Physical properties of the soil mixtures

Density of fluid	ρ_f	1.0 g/cm^3
Density of solids	ρ_s	2.65 g/cm^3
Kinematic viscosity of fluid	η_k	5.0×10^{-6} m^{2}s^{-1}
Minimum porosity	ϕ_{min}	0.22

Table 3 Values of model parameters for tested soil mixtures A, B and C

Tests	Erosion parameters			Filtration parameters		Permeability parameter
	λ_e	α_1	α_2	λ_f	β	m
Series A	151.6	0.89	3.42	170.6	1.0	16
Series B	3.1	0.74	2.68	13.4	1.0	16

4.1.2. Results

Fig. 4 presents the comparison between experimental and numerical results of erosion tests on three types of soil mixtures in the case of hydraulic loadings (a) and (b). It shows that the history of the hydraulic loading and the initial fine content affect significantly the hydraulic behavior of the tested soil mixtures. Two phases can be distinguished from the time evolution of the hydraulic conductivity. At first, the hydraulic conductivity slowly increased or decreased, depending on the hydraulic loading type. The duration of this first phase was much longer under less severe hydraulic loading. For a given hydraulic loading, the decreasing phase was longer for a specimen with a smaller initial fine content. These results illustrate a positive correlation between the erosion rate and the initial fine content. The second phase of the hydraulic conductivity evolution was characterized by its rapid increase. Finally, the hydraulic conductivity reached a constant value.

The proposed model was able to reproduce the two phases of the erosion until a stable stage was reached. However, in some cases, discrepancies between experimental and numerical hydraulic conductivity evolution could be found, especially during the first phase. Only few data are available in the literature concerning the self-filtration phenomenon during an erosion test. Ke and Takahashi [26,57] attributed the deviation of the hydraulic conductivity to the difference in homogeneity along the reconstituted soil specimens. Another aspect which has not been taken into account is the unknown influence of the saturation stage, which may also lead to the heterogeneity of the soil sample before erosion. The influence of the soil heterogeneity is discussed in the following section.

The predicted eroded mass can be calculated by [32]:

$$\Delta M = \rho_s \int_0^L \left[\phi(1-c) - \phi_0 (1-c_0) \right] dx \tag{34}$$

Marot et al. [22] proposed an energy-based method to characterize the erosion susceptibility. The authors suggested characterizing the fluid loading by the total flow power P_{flow}, expressed as

$$P_{\text{flow}} = q_w \gamma_w \Delta h \tag{35}$$

where q_w is the flow rate; γ_w is the unit weight of water; Δh is the drop of hydraulic head. In series A, Rochim et al. [23] characterized the evolution of the cumulative eroded mass with the variation of the cumulative expended energy E_{flow}, computed by the time integration of the instantaneous flow power P_{flow}.

Experimental and numerical values of the eroded mass are in good agreement for the calibration tests C97-a and C97-b, but also for other validation tests differing from the initial fine content and the hydraulic loading history. However, the prediction of the eroded mass is not totally in agreement with the experimental data for tests A90-a and A90-b. The eroded masses represent only 0.4% (test A90-a) and 1.2% (test A90-b) of their initial fine content, whereas the hydraulic conductivity increased by a factor of 9 (test A90-a) and 4 (test A90-b) in the second phase of the hydraulic conductivity evolution. Obviously, such small loss mass should not in itself result in such a rapid increase of the hydraulic conductivity. This discrepancy could be explained by the early presence of preferential flows created by particle rearrangements in the case of a lower initial fine content of the soil.

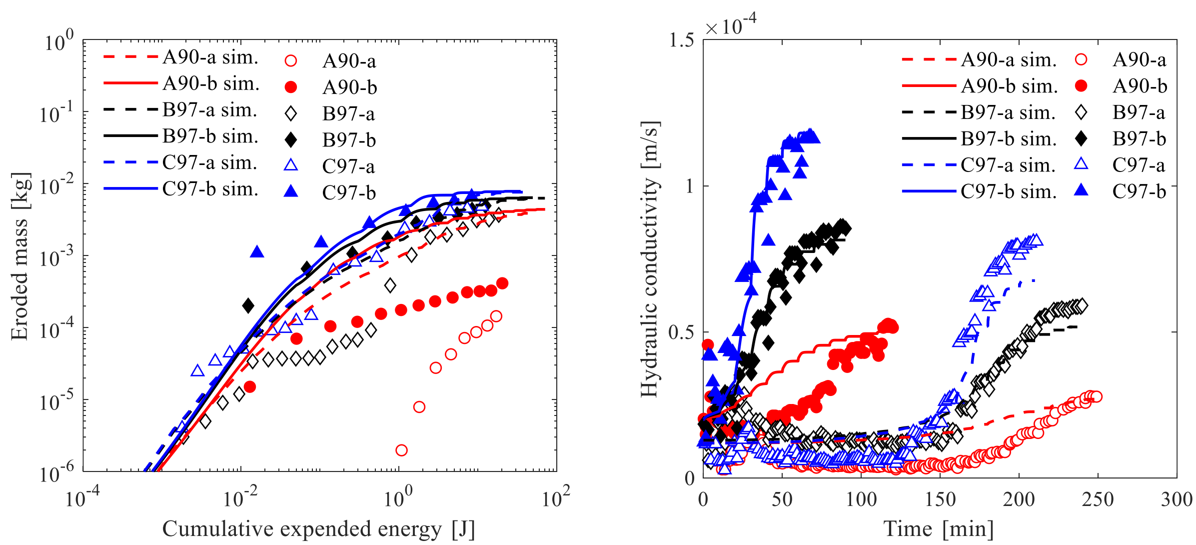

(a) (b)

Fig. 4 Comparison between laboratory tests (symbols) and simulated data (continuous lines): (a) cumulative eroded masses versus cumulative expended energy; (b) time evolution of hydraulic conductivity

4.2. Series B

Similar erosion tests on gap-graded mixtures of coarse and fine silica Hostun sand were performed by Aboul Hosn [54] to investigate the effects of the soil density on suffusion. The suffusion tests were carried out using a newly developed permeameter made up of a cylindrical Plexiglass cell (140 mm in height and 70 mm in internal diameter), a pressurized water supply system and a fine collector. Three soil samples with the same initial fine content (fc=25%) and three different relative densities (Id=0.2, 0.4, 0.6) were subjected to erosion tests by flushing water in the downward direction under a controlled multi-stage flow rate. The model parameters summarized in Table 3, were calibrated by fitting simultaneously the evolution of the hydraulic conductivity and the cumulative loss of dry mass of test ES-0.2-CD (shown by the red lines in Fig. 5) by trial-error which can be alternatively identified using optimization technique. They were then used to predict the other tests.

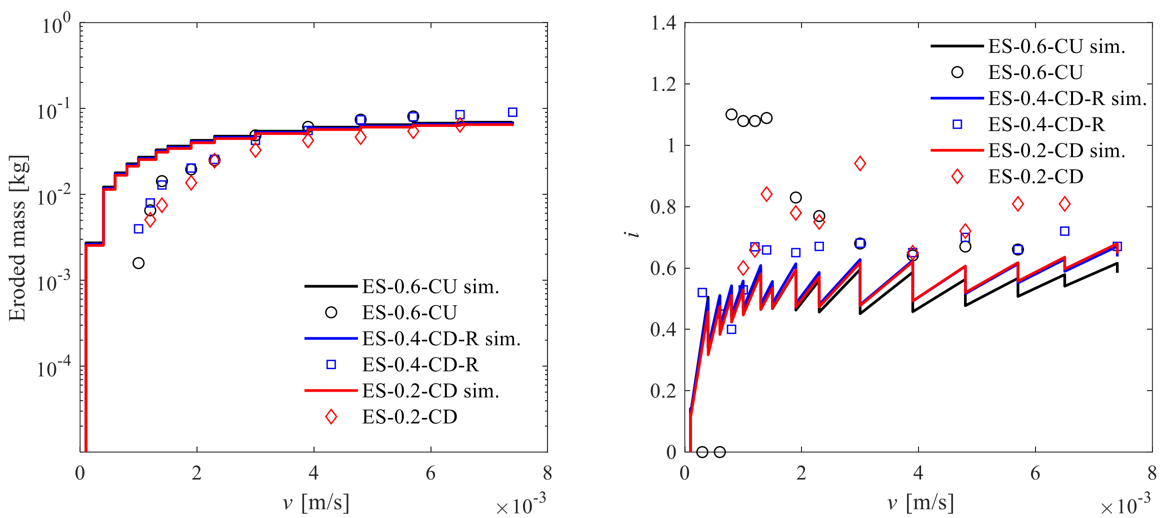

(a) (b)

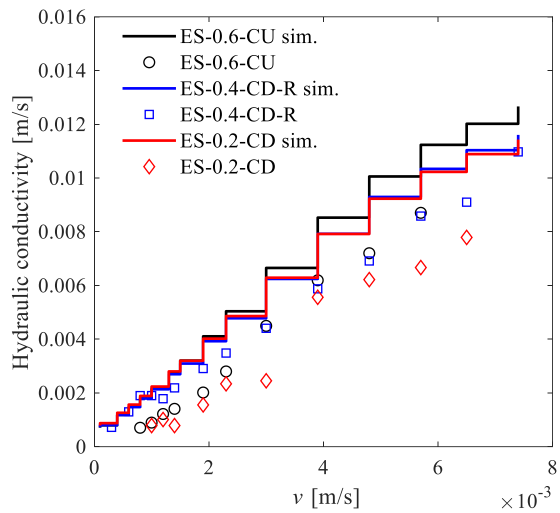

(c)

Fig. 5 Comparison between laboratory tests (symbols) and simulated data (continuous lines) for three different initial densities: (a) the variation of cumulative eroded masses with the increasing flow rate; (b) the variation of hydraulic gradient, *i*, with the increasing flow rate; (c) the variation of hydraulic conductivity with the increasing flow rate

The comparison between experimental and numerical results of the erosion tests with three different relative densities (Id=0.2, 0.4, 0.6) is presented in Fig. 5. The curves show similar tendencies. With the increase in Darcy's flow velocity, the eroded mass increased with time at a gradual decrease rate. The deviations of the experimental results appear to be very small, possibly due to the minor differences of their initial porosity (0.36, 0.34, 0.32 for Id=0.2, 0.4, 0.6, respectively). The proposed model was able to capture the main features of the flow-rate controlled erosion tests.

5. Discussion

Comparing the time evolution of the hydraulic conductivity with the measured eroded mass constitutes a way to improve the understanding of the suffusion process. Fig. 6 shows how the numerical results depend on the choice of the parameter β which controls the filtration rate (Eq. 22). The complex phenomenon of suffusion appears to be a combination of three processes: detachment, transport, and filtration of the finer fraction. This combination results in the development of heterogeneities in the soil grading. Experimental results [23,58] showed that the loss of fine particles is higher in the upstream part. The transport of detached particles from upstream to downstream can partly offset the loss of particles in the downstream region. The spatial profiles of porosity at different time steps for different values of β are compared in Fig. 7. A larger value of β leads to a more severe soil heterogeneity at the early stage of the suffusion, which suggests that more detached particles are filtered in the downstream part of the soil. However, to calibrate the value of β, it is necessary to measure the concentration of fluidized particle within the outlet flow at discrete times during an experiment. Under a given hydraulic gradient condition, a strong increase of the concentration of fluidized particle in the outlet flow occurs simultaneously to the rapid increase of the hydraulic conductivity, as shown in Fig. 8. For a given density, a lower fine content is accompanied by a larger amount of coarse particles and a smaller constriction size within the porous network, which facilitates the filtration process.

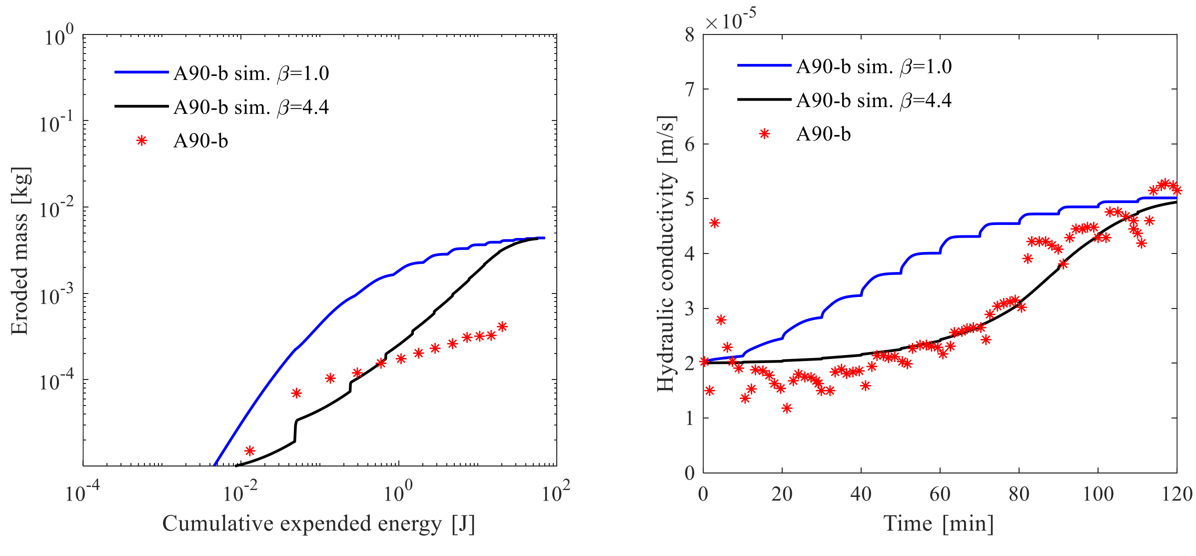

(a) (b)

Fig. 6 Comparison between laboratory tests (symbols) and simulated data (continuous lines) for different values of β: (a) cumulative eroded masses versus cumulative expended energy; (b) time series of hydraulic conductivity

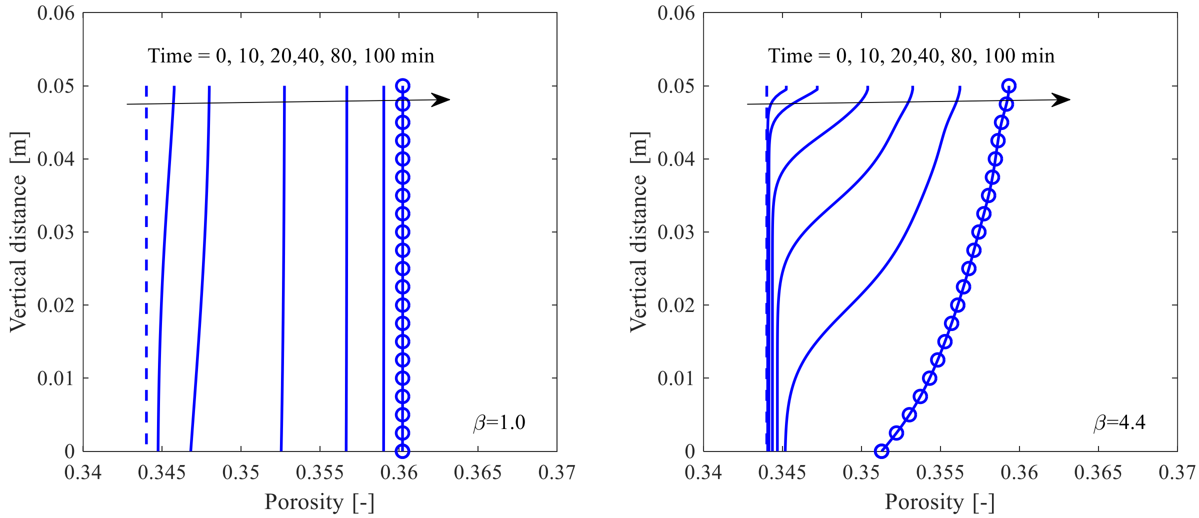

(a) (b)

Fig. 7 Spatial profiles of porosity at various time steps: (a) $\beta = 3.0$; (b) $\beta = 6.4$

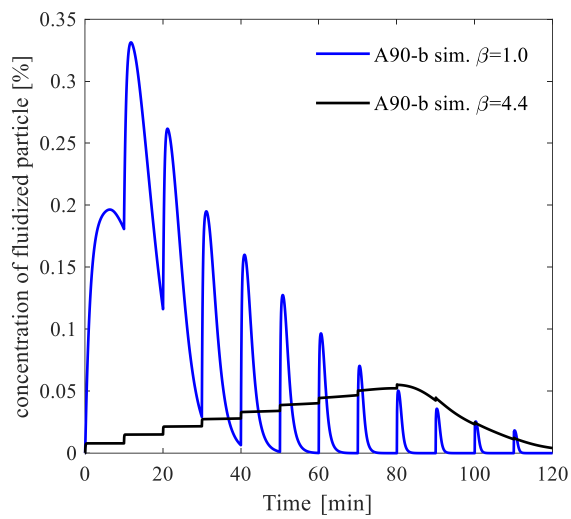

Fig. 8 Comparison of the concentration of fluidized particle of the outlet flow for different values of β

The rapid decrease of the hydraulic conductivity is systematically accompanied by a clogging of the pores. The compaction of the reconstituted soil specimens and the disturbance during the saturation stage may lead to initially heterogeneous soil samples. Fine particles that are displaced can fill certain pores during compaction and saturation. Fig. 10 compares experimental and numerical results for different soil homogeneities. The initial fine content and the corresponding porosity are presented in Fig. 9.

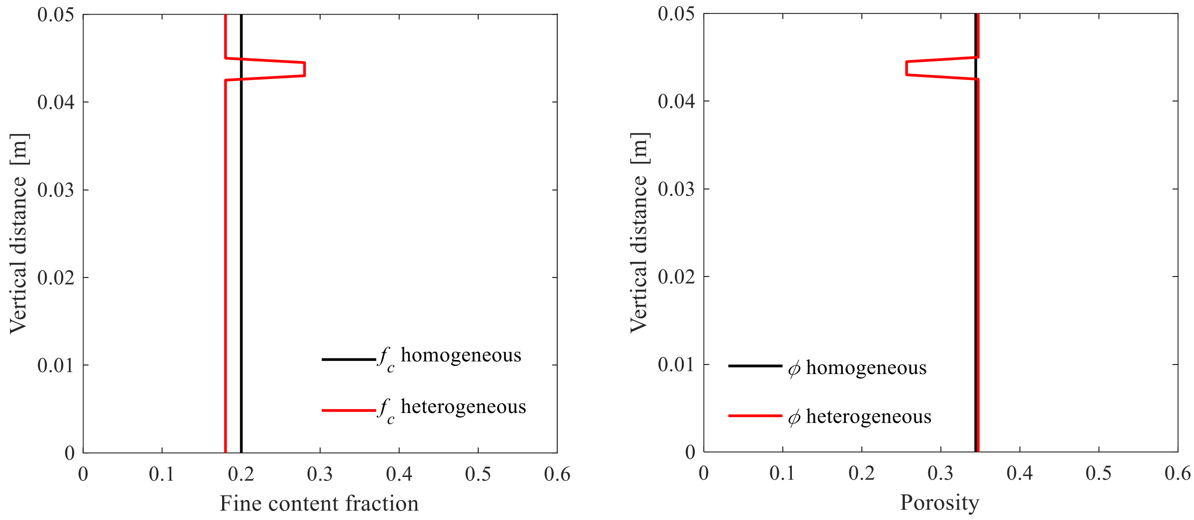

(a) (b)

Fig. 9 Initial soil state before erosion for different soil homogeneity: (a) initial fine content fraction; (b) initial porosity

A clogging, at first restricting the water flow, can then be blown away, accompanied by a significant increase of the hydraulic conductivity. Thus, the predominant process during the second phase is the detachment and transport of fine particles. Finally, the hydraulic conductivity tends to stabilize when the hydraulic drag force can no longer transport any more fine particles through the soil skeleton.

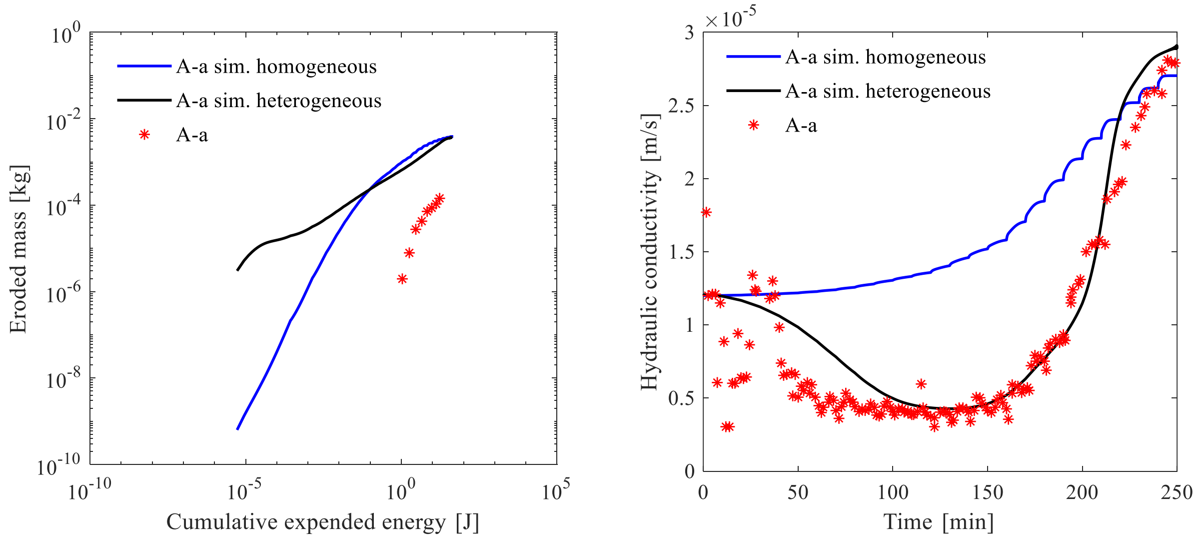

(a) (b)

Fig. 10 Comparison between laboratory tests (symbols) and simulated data (continuous lines) for different soil homogeneity: (a) cumulative eroded masses versus cumulative expended energy; (b) time series of hydraulic conductivity

6. Conclusion

This study provided a novel contribution to the numerical approach in modeling the internal erosion of soils. The approach consisted of modeling the erosion of the soil skeleton, the transport by the water flow and the filtration of fine particles through the mass exchange between the solid and fluid phases. The governing differential equations were formulated based on the mass balance of four assumed constituents: the stable fabric of the solid skeleton, the erodible fines, the fluidized particles, and the pure fluid. The terms of mass exchange were introduced into the mass balance equations. It was complemented by a filtration term to simulate the filling of initial voids due to the filtration of transported fines from the suspension to the solid fraction. The model was solved numerically by a finite difference method restricted to 1-D flows normal to the free surface and, accordingly, the hydrodynamic dispersion was disregarded.

Two series of erosion tests on cohesionless soils were selected in order to examine the model performance. Two phases of the suffusion process up to a stable stage could be distinguished from the time evolution of the hydraulic conductivity and both were well reproduced by the model. The hydraulic conductivity first slowly increased, or even decreased, depending on the hydraulic loading history. The second phase of the hydraulic conductivity evolution was characterized by a rapid increase. Finally, the hydraulic conductivity reached a constant value. The results showed that the numerical model is able to describe both erosion and filtration during the tests.

A complementary study on the coupling between erosion and filtration indicated that a larger value of the parameter β controlling the amplitude of filtration leads to a more severe soil heterogeneity at the early stage of the erosion, which suggests that more detached particles are filtered in the downstream part of the soil. Thus, the hydraulic conductivity of the whole specimen could slowly increase or decrease. The second phase of the hydraulic conductivity evolution characterized by a rapid increase occurs simultaneously with the unblocking of the clogged pores. Finally, the hydraulic conductivity reaches a constant value when the hydraulic force is no longer able to drag fine particles through the soil skeleton.

Note that the proposed numerical approach is formulated for the boundary value problems at the scale of an entire engineering structure for gap-graded or broadly graded granular soils. The grain-scale or particle size distribution related parameters were not considered for the sake of simplicity. In future works, the grain-scale parameters will be calibrated and introduced into the erosion law or filtration law based on well documented experimental tests; the coupling model will also be extended to 3D conditions so that more complex geometries and boundary conditions can be treated for a soil mass subjected to suffusion.

Acknowledgement

The financial supports provided by the National Institute for Industrial Environment and Risks of France (INERIS) and the National Natural Science Foundation of China (51579179) are gratefully acknowledged.

Appendix A. Finite difference solution for 1D suffusion process

Defining $r_1 = \Delta t / (\Delta x)^2$ and $r_2 = \Delta t / \Delta x$ allows the Eqs.(31)-(33) to be rewritten

$$-r_1\left[A_{p_w}\right]_{j-1/2}^{k} p_{w\,j-1}^{\,k+1} + \left\{1+r_1\left(\left[A_{p_w}\right]_{j-1/2}^{k}+\left[A_{p_w}\right]_{j+1/2}^{k}\right)\right\} p_{w\,j}^{\,k+1} - r_1\left[A_{p_w}\right]_{j+1/2}^{k} p_{w\,j+1}^{\,k+1} = p_{w\,j}^{\,k} \tag{36}$$

with

$$\left[A_{p_w}\right]_{j-1/2}^{k} = \left(\frac{0.5}{\left[A_{p_w}\right]_{j-1}^{k}}+\frac{0.5}{\left[A_{p_w}\right]_{j}^{k}}\right)^{-1},\ \left[A_{p_w}\right]_{j+1/2}^{k} = \left(\frac{0.5}{\left[A_{p_w}\right]_{j}^{k}}+\frac{0.5}{\left[A_{p_w}\right]_{j+1}^{k}}\right)^{-1},\ \left[A_{p_w}\right]_{j}^{k} = \left[\frac{Ek\left(f_c,\phi\right)}{\eta\bar{\rho}\left(c\right)}\right]_{j}^{k}$$

$$-r_2A_\phi\phi_{j-1}^{k+1} + \left(1+r_2A_\phi\right)\phi_j^{k+1} = \left(1-\Delta t B_\phi\right)\phi_j^k - \Delta t C_\phi \tag{37}$$

with

$$A_\phi = \frac{u_j^{k+1}-u_j^k}{\Delta t},\ B_\phi = -\frac{\varepsilon_{v\,j}^{\,k+1}-\varepsilon_{v\,j}^{\,k}}{\Delta t},\ C_\phi = \frac{\varepsilon_{v\,j}^{\,k+1}-\varepsilon_{v\,j}^{\,k}}{\Delta t} + \left[\left(-\lambda_e\left(1-\phi\right)\left(f_c-f_{c\infty}\right)+\lambda_f\frac{\phi-\phi_{\min}}{\phi^\beta}c\right)\left|q_w\right|\right]_j^k$$

$$-r_2A_c c_{j-1}^{k+1} + \left(1+r_2A_c\right)c_j^{k+1} = \left(1-\Delta t B_c\right)c_j^k - \Delta t C_c \tag{38}$$

with

$$A_c = \left(\left[\frac{q_w}{\phi}\right]_j^k + \frac{u_j^{k+1}-u_j^k}{\Delta t}\right),\ B_c = \frac{1}{\phi_j^k}\left(\frac{\phi_j^{k+1}-\phi_j^k}{\Delta t} + \left[\operatorname{div}\left(q_w\right)\right]_j^k + \frac{\phi_{j+1}^k-\phi_{j-1}^k}{2\Delta x}\frac{u_j^{k+1}-u_j^k}{\Delta t} - \phi_j^k\frac{\varepsilon_{v\,j}^{\,k+1}-\varepsilon_{v\,j}^{\,k}}{\Delta t}\right),$$

$$C_c = \left[\left(-\lambda_e\left(1-\phi\right)\left(f_c-f_{c\infty}\right)+\lambda_f\frac{\phi-\phi_{\min}}{\phi^\beta}c\right)\left|q_w\right|\Big/\phi\right]_j^k$$

where $\left(j=1,2,3...,N-1;k=1,2,3...,M-1\right)$.

References

1. Foster M, Fell R, Spannagle M (2000) The statistics of embankment dam failures and accidents. Canadian Geotechnical Journal 37 (5):1000-1024
2. Fell R, Fry J-J (2007) The state of the art of assessing the likelihood of internal erosion of embankment dams, water retaining structures and their foundations. Internal Erosion of Dams and their Foundations, Robin Fell & Jean-Jacques Fry–editors, Taylor & Francis
3. Fry J-J, Vogel A, Royet P, Courivaud J-R (2012) Dam failures by erosion: lessons from ERINOH data bases. ICSE6 Paris:273-280
4. Shen S-L, Xu Y-S (2011) Numerical evaluation of land subsidence induced by groundwater pumping in Shanghai. Canadian Geotechnical Journal 48 (9):1378-1392

5. Shen S, Wang Z, Cheng W (2017) Estimation of lateral displacement induced by jet grouting in clayey soils. Geotechnique 67 (7):621-630

6. Wu H-N, Shen S-L, Yang J (2017) Identification of tunnel settlement caused by land subsidence in soft deposit of Shanghai. Journal of Performance of Constructed Facilities 31 (6):04017092

7. Lei X, Yang Z, He S, Liu E, Wong H, Li X (2017) Numerical investigation of rainfall-induced fines migration and its influences on slope stability. Acta Geotechnica 12 (6):1431-1446

8. Hu W, Hicher P-Y, Scaringi G, Xu Q, Van Asch T, Wang G (2018) Seismic precursor to instability induced by internal erosion in loose granular slopes. Géotechnique:1-13

9. Fell R, Wan CF, Cyganiewicz J, Foster M (2003) Time for development of internal erosion and piping in embankment dams. Journal of geotechnical and geoenvironmental engineering 129 (4):307-314

10. Wan CF, Fell R (2004) Investigation of rate of erosion of soils in embankment dams. Journal of geotechnical and geoenvironmental engineering 130 (4):373-380

11. Bonelli S, Marot D On the modelling of internal soil erosion. In: The 12th International Conference of International Association for Computer Methods and Advances in Geomechanics (IACMAG), 2008. p 7

12. Chang CS, Yin Z-Y (2011) Micromechanical modeling for behavior of silty sand with influence of fine content. International Journal of Solids and Structures 48 (19):2655-2667

13. Yin Z-Y, Zhao J, Hicher P-Y (2014) A micromechanics-based model for sand-silt mixtures. International journal of solids and structures 51 (6):1350-1363

14. Yin Z-Y, Huang H-W, Hicher P-Y (2016) Elastoplastic modeling of sand–silt mixtures. Soils and Foundations 56 (3):520-532

15. Skempton A, Brogan J (1994) Experiments on piping in sandy gravels. Geotechnique 44 (3):449-460

16. Reddi LN, Lee I-M, Bonala MV (2000) Comparison of internal and surface erosion using flow pump tests on a sand-kaolinite mixture. Geotechnical Testing Journal 23 (1):116-122

17. Sterpi D (2003) Effects of the erosion and transport of fine particles due to seepage flow. international journal of Geomechanics 3 (1):111-122

18. Bendahmane F, Marot D, Rosquoët F, Alexis A (2006) Characterization of internal erosion in sand kaolin soils: Experimental study. Revue européenne de génie civil 10 (4):505-520

19. Bendahmane F, Marot D, Alexis A (2008) Experimental parametric study of suffusion and backward erosion. Journal of Geotechnical and Geoenvironmental Engineering 134 (1):57-67

20. Moffat R, Fannin RJ, Garner SJ (2011) Spatial and temporal progression of internal erosion in cohesionless soil. Canadian Geotechnical Journal 48 (3):399-412

21. Chang D, Zhang L (2011) A stress-controlled erosion apparatus for studying internal erosion in soils. Geotechnical Testing Journal 34 (6):579-589

22. Marot D, Rochim A, Nguyen H-H, Bendahmane F, Sibille L (2016) Assessing the susceptibility of gap-graded soils to internal erosion: proposition of a new experimental methodology. Natural Hazards 83 (1):365-388

23. Rochim A, Marot D, Sibille L, Thao Le V (2017) Effects of Hydraulic Loading History on Suffusion Susceptibility of Cohesionless Soils. Journal of Geotechnical and Geoenvironmental Engineering 143 (7):04017025

24. Sherard JL, Dunnigan LP, Talbot JR (1984) Filters for silts and clays. Journal of Geotechnical Engineering 110 (6):701-718

25. Kenney T, Chahal R, Chiu E, Ofoegbu G, Omange G, Ume C (1985) Controlling constriction sizes of granular filters. Canadian Geotechnical Journal 22 (1):32-43
26. Ke L, Takahashi A (2014) Experimental investigations on suffusion characteristics and its mechanical consequences on saturated cohesionless soil. Soils and Foundations 54 (4):713-730
27. Kenney T, Lau D (1985) Internal stability of granular filters. Canadian geotechnical journal 22 (2):215-225
28. Wan CF, Fell R (2008) Assessing the potential of internal instability and suffusion in embankment dams and their foundations. Journal of Geotechnical and Geoenvironmental Engineering 134 (3):401-407
29. Chang DS, Zhang LM (2013) Extended internal stability criteria for soils under seepage. Soils and Foundations 53 (4):569-583
30. Indraratna B, Israr J, Rujikiatkamjorn C (2015) Geometrical method for evaluating the internal instability of granular filters based on constriction size distribution. Journal of Geotechnical and Geoenvironmental Engineering 141 (10):04015045
31. Wennberg KE, Batrouni G, Hansen A Modelling fines mobilization, migration and clogging. In: SPE European Formation Damage Conference, 1995. Society of Petroleum Engineers,
32. Vardoulakis I, Stavropoulou M, Papanastasiou P (1996) Hydro-mechanical aspects of the sand production problem. Transport in porous media 22 (2):225-244
33. Papamichos E, Vardoulakis I, Tronvoll J, Skjaerstein A (2001) Volumetric sand production model and experiment. International journal for numerical and analytical methods in geomechanics 25 (8):789-808
34. Stavropoulou M, Papanastasiou P, Vardoulakis I (1998) Coupled wellbore erosion and stability analysis. International journal for numerical and analytical methods in geomechanics 22 (9):749-769
35. Cividini A, Gioda G (2004) Finite-element approach to the erosion and transport of fine particles in granular soils. International Journal of Geomechanics 4 (3):191-198
36. Fujisawa K, Murakami A, Nishimura S-i (2010) Numerical analysis of the erosion and the transport of fine particles within soils leading to the piping phenomenon. Soils and foundations 50 (4):471-482
37. Bear J, Bachmat Y (2012) Introduction to modeling of transport phenomena in porous media, vol 4. Springer Science & Business Media,
38. Wong H, Zhang X, Leo C, Bui T (2013) Internal Erosion of earth structures as a coupled hydromechanical process. Paper presented at the Applied Mechanics and Materials,
39. Schaufler A, Becker C, Steeb H (2013) Infiltration processes in cohesionless soils. ZAMM ‐ Journal of Applied Mathematics and Mechanics/Zeitschrift für Angewandte Mathematik und Mechanik 93 (2 ‐ 3):138-146
40. Sato M, Kuwano R (2015) Suffusion and clogging by one-dimensional seepage tests on cohesive soil. Soils and Foundations 55 (6):1427-1440
41. Reboul N, Vincens E, Cambou B (2010) A computational procedure to assess the distribution of constriction sizes for an assembly of spheres. Computers and Geotechnics 37 (1-2):195-206
42. Reboul N (2008) Transport de particules dans les milieux granulaires: Application à l'érosion interne. Ecully, Ecole centrale de Lyon,
43. Scholtès L, Hicher P-Y, Sibille L (2010) Multiscale approaches to describe mechanical responses induced by particle removal in granular materials. Comptes Rendus Mécanique 338 (10-11):627-638

44. Lominé F, Scholtès L, Sibille L, Poullain P (2013) Modeling of fluid–solid interaction in granular media with coupled lattice Boltzmann/discrete element methods: application to piping erosion. International Journal for Numerical and Analytical Methods in Geomechanics 37 (6):577-596
45. Zhao J, Shan T (2013) Coupled CFD–DEM simulation of fluid–particle interaction in geomechanics. Powder technology 239:248-258
46. Sibille L, Lominé F, Poullain P, Sail Y, Marot D (2015) Internal erosion in granular media: direct numerical simulations and energy interpretation. Hydrological Processes 29 (9):2149-2163
47. Sari H, Chareyre B, Catalano E, Philippe P, Vincens E Investigation of internal erosion processes using a coupled dem-fluid method. In: Particles 2011 II International Conference on Particle-Based Methods, E. Oate and DRJ Owen (Eds), Barcelona, 2011. pp 1-11
48. Zou Y-H, Chen Q, Chen X-Q, Cui P (2013) Discrete numerical modeling of particle transport in granular filters. Computers and Geotechnics 47:48-56
49. Wang M, Feng Y, Pande G, Chan A, Zuo W (2017) Numerical modelling of fluid-induced soil erosion in granular filters using a coupled bonded particle lattice Boltzmann method. Computers and Geotechnics 82:134-143
50. Uzuoka R, Ichiyama T, Mori T, Kazama M Hydro-mechanical analysis of internal erosion with mass exchange between solid and water. In: 6th International Conference on Scour and Erosion, 2012. pp 655-662
51. Cividini A, Bonomi S, Vignati GC, Gioda G (2009) Seepage-induced erosion in granular soil and consequent settlements. International Journal of Geomechanics 9 (4):187-194
52. Revil A, Cathles L (1999) Permeability of shaly sands. Water Resources Research 35 (3):651-662
53. Guide MUs (1998) The mathworks. Inc, Natick, MA 5:333
54. Aboul Hosn R (2017) Suffusion and its effects on the mechanical behavior of granular soils: numerical and experimental investigations. Grenoble Alpes,
55. Jin YF, Yin ZY, Shen SL, Hicher PY (2016) Selection of sand models and identification of parameters using an enhanced genetic algorithm. International Journal for Numerical and Analytical Methods in Geomechanics 40 (8):1219-1240
56. Yin ZY, Jin YF, Shen JS, Hicher PY (2018) Optimization techniques for identifying soil parameters in geotechnical engineering: Comparative study and enhancement. International Journal for Numerical and Analytical Methods in Geomechanics 42 (1):70-94
57. Ke L, Takahashi A (2014) Triaxial erosion test for evaluation of mechanical consequences of internal erosion. Geotechnical Testing Journal 37 (2):347-364
58. Ke L, Takahashi A (2012) Strength reduction of cohesionless soil due to internal erosion induced by one-dimensional upward seepage flow. Soils and Foundations 52 (4):698-711

Figure captions

Fig. 11 REV of a fully-saturated soil mixture and the four-constituent continuum model

Fig. 12 Geometry and finite difference grid in space-time of analyzed 1-D internal erosion

Fig. 13 Time evolution of multi-staged hydraulic gradients

Fig. 14 Comparison between laboratory tests (symbols) and simulated data (continuous lines): (a) cumulative eroded masses versus cumulative expended energy; (b) time evolution of hydraulic conductivity

Fig. 15 Comparison between laboratory tests (symbols) and simulated data (continuous lines) for three different initial densities: (a) the variation of cumulative eroded masses with the increasing flow rate; (b) the variation of hydraulic gradient, i, with the increasing flow rate; (c) the variation of hydraulic conductivity with the increasing flow rate

Fig. 16 Comparison between laboratory tests (symbols) and simulated data (continuous lines) for different values of β: (a) cumulative eroded masses versus cumulative expended energy; (b) time series of hydraulic conductivity

Fig. 17 Spatial profiles of porosity at various time steps: (a) $\beta = 3.0$; (b) $\beta = 6.4$

Fig. 18 Comparison of the concentration of fluidized particle of the outlet flow for different values of β

Fig. 19 Initial soil state before erosion for different soil homogeneity: (a) initial fine content fraction; (b) initial porosity

Fig. 20 Comparison between laboratory tests (symbols) and simulated data (continuous lines) for different soil homogeneity: (a) cumulative eroded masses versus cumulative expended energy; (b) time series of hydraulic conductivity

Table 4 properties of simulated test specimens

Soil reference	Specimen reference	Initial dry density γ_d (kN/m^3)	Initial permeability k (m/s)	Applied hydraulic gradient, i	Test duration (min)
A	A90-a	17.39	1.2×10^{-5}	Type a, from 0.1 to 15	270
	A90-b	17.39	2.0×10^{-5}	Type b, from 1 to 13	130
B	B97-a	18.74	1.3×10^{-5}	Type a, from 0.1 to 12	240
	B97-b	18.74	2.0×10^{-5}	Type b, from 1 to 9	90
C	C97-a	18.74	1.2×10^{-5}	Type a, from 0.1 to 9	210
	C97-b	18.74	2.0×10^{-5}	Type b, from 1 to 7	70

Table 5 Physical properties of the soil mixtures

Density of fluid	ρ_f	1.0 g/cm^3
Density of solids	ρ_s	2.65 g/cm^3
Kinematic viscosity of fluid	η_k	5.0×10^{-6} m^{2}s^{-1}
Minimum porosity	$\phi_{\min}$	0.22

Table 6 Values of model parameters for tested soil mixtures A, B and C

Tests	Erosion parameters				Filtration parameters			Permeability parameters
	λ_e	α_1	α_2		λ_f	β		m
Series A	151.6	0.89	3.42		170.6	1.0		16
Series B	3.1	0.74	2.68		13.4	1.0		16